ACS SENSORS

pubs.acs.org/acssensors Article

Smart Garment for Continuous Respiration Monitoring in Canines

Seokkyoon Hong,[‖] Taewoong Park,[‖] Youngjun Lee,[‖] Juan C. Mesa, Tianhao Yu, Yuhyun Ji, Junsang Lee, Jinheon Jeong, Seok-Won Kang, Dong Rip Kim, Young L. Kim, Hyowon Lee, Rachel K. Surowiec,* Luis Dos Santos,* and Chi Hwan Lee*

Cite This: https://doi.org/10.1021/acssensors.5c03783 Read Online

ABSTRACT: There is a growing need for at-home respiration monitoring in canines, who are prone to respiratory issues due to breed-specific anatomy and active lifestyles. Continuous monitoring of respiration provides critical insight into stress and illness; however, current solutions—ranging from clinical instruments to wearable devices—are either accurate but invasive and episodic or limited in fit and comfort. Here, we introduce a smart garment that integrates a spongy-like strain sensor and compact data acquisition module into commercially available canine apparel, enabling continuous, non-invasive monitoring of respiration, body temperature, and physical activity. Validation with two breeds, Labrador and Boxer, confirmed its ability to capture breed- and activity-specific respiration patterns, including differences in breathing rate, amplitude, and panting behavior. Using convolutional neural network (CNN)-assisted machine learning (ML), the system classified respiratory patterns across breeds and activity levels with over 94.3% accuracy. Beyond canines, this platform may hold potential for future adaptation to other companion animals, such as cats, suggesting a broader scope for home-based veterinary monitoring.

KEYWORDS: *wearable biomedical devices, veterinary telehealth, smart garment, machine learning, respiration monitoring in companion animals*

The growing recognition of companion animals—such as dogs and cats—as integral members of the family underscores the need for continuous, home-based health monitoring systems that support early detection and management of disease.[1−3] Among various physiological indicators, respiration serves as a particularly valuable biomarker, offering early insight into respiratory dysfunction, cardiac conditions, stress, and systemic illness.[4−6] While both dogs and cats are susceptible to respiratory disorders, dogs face higher risks due to their breed diversity, active lifestyles, and anatomical predispositions—especially in brachycephalic breeds such as pugs and bulldogs.[7−9] In addition, frequent outdoor activities and social interactions increase their exposure to airborne pathogens and environmental triggers, making respiratory monitoring critical for canine health.[9] This challenge is compounded by the fact that animals cannot verbalize discomfort, and clinical signs often emerge only after substantial decline.[10]

Current clinical standards for assessing respiration in dogs include capnography during anesthesia and arterial blood gas analysis via arterial puncture.[11−14] These methods require specialized equipment and trained personnel, making them invasive, costly, and impractical for routine use outside clinical settings.[11,12] Non-invasive methods—such as visual observation and auscultation—are more accessible but limited by inter-operator variability, relying on practitioner experience.[15] Respiratory assessments using face masks can improve measurement accuracy but are poorly tolerated by dogs due to interference with natural behaviors like eating or grooming.[16−19] Signs of discomfort, stress, or allergic reaction may also occur.[20] Moreover, these assessments require in-clinic visits, which can be time-consuming and financially burdensome.[21,22]

Despite rapid progress in wearable respiratory monitoring technologies for humans, comparable solutions for companion animals remain scarce.[23−26] This is largely due to anatomical variability, limited market incentives, and user compliance challenges.[27,28] Some wearable devices—such as respiratory harnesses, straps, and collars—have been developed to support non-invasive, real-time monitoring outside clinical settings.[29−31] These devices hold promise for detecting respiratory distress, supporting post-operative recovery, and enabling health tracking in home environments. However, their use still faces challenges related to comfort, fit, and tolerability.[32−35] For example, harnesses and chest straps are often not fitted: one survey reported 82% of 1567 dog owners did not have their harness adjusted.[32] Suboptimal

Received: October 12, 2025
Revised: February 20, 2026
Accepted: February 23, 2026

fit may contribute to signal variability and injury to the fur.[33] In particular, limited contact areas can concentrate pressure, increasing risk of localized injury.[34] Furthermore, loose collars may allow dogs to slip out, while tight configurations could introduce choking.[35] These factors can affect both animal welfare and data quality, reducing compliance and making continuous home monitoring difficult.[36,37] Representative veterinary wearables are compared with our smart clothing in Table S1.[31,34,38,39]

Here, we introduce a smart garment that fully integrates a spongy-like strain sensor and data acquisition (DAQ) modules into commercially available canine apparel. Unlike respiratory harnesses or face masks, this design preserves the original comfort, flexibility, and wearability of standard dog garments, enabling continuous and unobtrusive monitoring in naturalistic settings. The platform supports multimodal physiological sensing, capturing respiration along with body temperature and physical activity as complementary health indicators. Leveraging machine learning (ML) algorithms, the collected data can be processed to classify respiratory patterns across different breeds and activity levels. In validation studies, the system demonstrated high classification accuracy of >94.3%, underscoring its potential for reliable, at-home respiratory tracking. Importantly, the smart garment is adaptable to different canine body types and sizes, ensuring a secure fit and comfort. Coupling this adaptability with its unobtrusive design and intelligent analytics, the platform may provide a scalable approach to continuous, non-invasive respiratory monitoring, with the possibility of extending to other companion animals in the future.

RESULTS AND DISCUSSION

AI-Assisted Smart Garment for Canine Health Monitoring

We developed a smart garment platform for continuous, multimodal canine health monitoring that integrates advanced wearable technologies while balancing functionality, durability, comfort, and the aesthetic qualities of commercially available apparel. The system unobtrusively records respiration, motion, and body temperature during natural activities, transmitting data wirelessly via Bluetooth Low Energy (BLE) to a mobile device for real-time monitoring (Figure 1a). Respiration signals are processed using machine learning (ML) models—such as random forest (RF), decision tree (DT), and extreme gradient boosting (XGBoost)—with features extracted through both convolutional neural networks (CNNs) and traditional ML methods, enabling differentiation of respiration patterns across breeds and activity levels for canine health monitoring. These ML classifiers were chosen for their proven effectiveness on structured, tabular data and their compatibility with post-hoc explainability methods such as SHAP, allowing for both high accuracy and interpretable predictions.[40]

In detail, the smart garment integrates three primary components: (1) a spongy-like strain sensor, (2) serpentine interconnectors, and (3) data acquisition (DAQ) modules (Figure 1b). The fabrication process of the smart garment is illustrated in Figure S1. Fabrication begins with designing the interconnectors in serpentine geometries using a computer-aided design (CAD)-guided cutting machine, followed by transfer onto the textile substrate. The hot-melt adhesive backing of the fabric enables robust bonding through simple ironing, eliminating the need for additional surface treatment. This serpentine layout evenly distributes mechanical stress (Figure S2a), maintaining compliance during natural motion. The spongy-like strain sensor, consisting of a microporous elastomer coated with carbon nanotubes (CNTs), is then affixed between two interconnectors with conductive paste, transducing respiration-induced strain into electrical signals. The spongy CNT foam is produced through a steam-etching process using a universal pressure rice cooker, yielding interconnected pores 5−50 μm in diameter (Figure S2b). This approach enables batch production (4 × 3 in.^{2} in 30 min) through a simple steam-etching step, avoiding solvent use and multi-step protocols typical of lithography or templating (Table S2).[41−43]

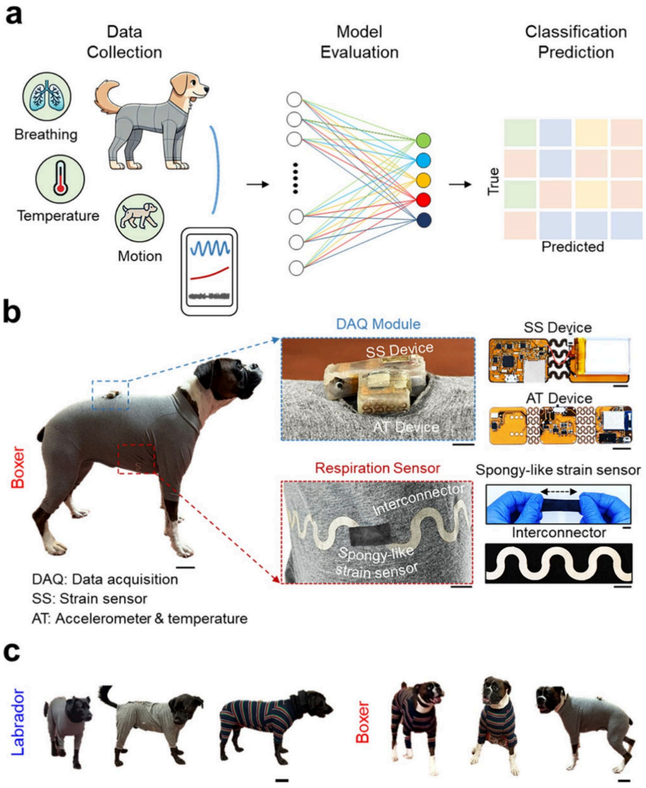

Figure 1. Smart garment for canine health monitoring and AI-based classification. (a) Schematic of the wearable system collecting respiration, temperature, and motion data, which are transmitted wirelessly and processed via an AI model to classify physiological states. (b) Photograph and detailed views of the smart garment worn by a dog, showcasing the locations and components of the DAQ modules, spongy-like strain sensor, and interconnectors used for real-time physiological monitoring. Scale bar for the dog, 10 cm. All other scale bars, 1 cm. (c) Photographs of Labrador and Boxer, wearing different types of garments in various postures. Scale bar, 10 cm.

The DAQ component includes two wearable devices: (1) a spongy-like strain sensor-integrated device (SS Device) and (2) a three-axis accelerometer/temperature sensor-integrated device (AT Device). The SS Device incorporates a flexible printed circuit board (fPCB) with 50 active and passive components, including a constant current source (LM234, Texas Instruments) supplying 110 μA and a BLE system-on-chip (nRF51822, Nordic Semiconductor), providing over 18 h of operation from a 350 mAh lithium-ion polymer battery. The AT Device contains 37 active and passive components, including a BMI160 three-axis accelerometer with integrated thermometer (Bosch) and a BLE system-on-chip (nRF52840, Nordic Semiconductor), offering 15 h of operation from a 150 mAh battery. For garment integration, a fabric band is inserted between the fPCB layers and secured to the garment with safety pins. Figure S3a displays the complete layout of the fPCB schematic, along with a detailed block diagram of the electronic subsystems depicted in Figure S3b. The use of commercially available garments (Figure 1c) ensures adaptability to different canine sizes and activity levels while maintaining wearer comfort and unobtrusiveness, ensuring adaptability and usability in practical settings.

Strain Sensing Performance

Figure 2a illustrates the stretchable spongy-like strain sensor, highlighting its porous architecture with percolating CNT networks that provide conductive pathways. The spongy-like strain sensor has shown a high porosity exceeding 80%, greater than typical ordered porous structures (<60%).[42] This highly porous architecture increases internal surface area, enabling stress dissipation through 3D pore wall rotation, thereby enhancing stability.[44]

The sensing performance is closely tied to the number of CNT infiltration cycles (IC). With increasing cycles, more CNTs are deposited along the pore walls (Figure S4a), systematically modulating both mechanical compliance and electrical conductivity. As ICs increase, the sensor exhibits reduced stretchability and higher modulus (Figures 2b, S4b,c), while electrical resistance and sensitivity decrease due to denser percolation pathways (Figure S4d). A single IC achieves the highest sensitivity (Figures 2c and S4e), whereas additional cycles stabilize the network but markedly reduce responsiveness (Figure S4f,g). Thus, the single-cycle sensor combines high sensitivity and stretchability, offering advantages over prior designs for wearable sensing (Figure S5).[45–47] Moreover, the strain sensing range and $\Delta R/R_0$ of the spongy-like strain sensor remained consistent regardless of sensor's size (Figure S6).

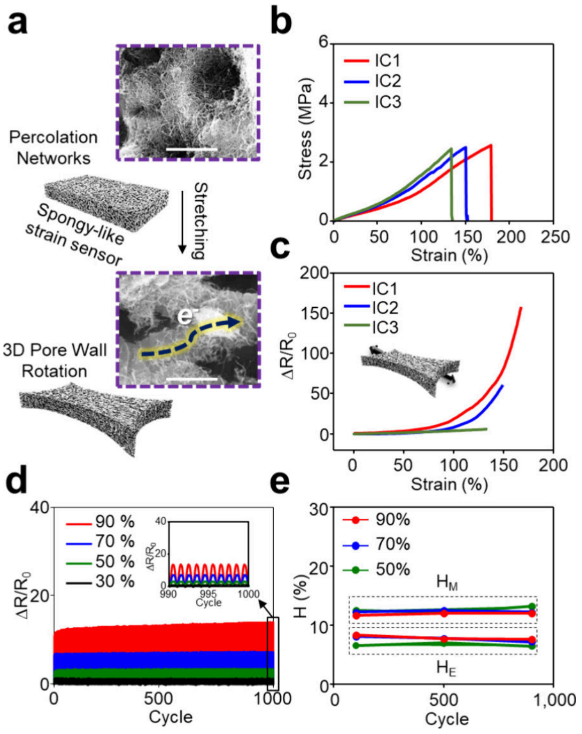

Figure 2. Strain sensing performance of a spongy-like strain sensor. (a) Schematic illustration of the spongy-like strain sensor, with enlarged insets showing the interconnected percolation network CNTs that serve as internal conductive pathways. Scale bar, 5 μm. (b) Stress−strain curves of the spongy-like strain sensor with different infiltration cycles. (c) $\Delta R/R_0$ of the spongy-like strain sensor with different infiltration cycles. (d) $\Delta R/R_0$ of the spongy-like strain sensor throughout 1000 stretching−releasing cycles with strains of 30, 50, 70, and 90%. (e) H_M and H_E of the spongy-like strain sensor with strains of 50, 70, and 90%.

For practical use, the sensor must withstand repeated loading.[48–50] As shown in Figure 2d, it maintained stable $\Delta R/R_0$ over 1000 stretch−release cycles at strains up to 90%. This durability arises from the 3D rotation of pore walls, which dissipates stress while preserving percolation pathways. The findings remained consistent for strains of 90% over 2000 cycles (Figure S7). Detailed photographs and SEM images of the spongy-like strain sensor are shown in Figure S8. This highlights its resilience under strain, contrasting with silver nanowire-based sensors that degrade beyond ∼50% strain.[44] The enhanced durability is attributed to the high fracture toughness of CNTs.[51]

The spongy-like strain sensor is selectively responsible for stretching that is decoupled from compression, due to its highly porous structure and percolated network of the CNTs. For example, the micropores of the spongy-like strain sensors can be closed when compressed without substantially altering the percolation pathways of the CNTs, resulting in minimal resistance changes (Figure S9).

The sensor also provides a consistent signal output during both loading and unloading, reducing calibration complexity.[52,53] Mechanical and electrical hysteresis were measured at 11.7−13.2% and 6.6−8.3%, respectively, influenced by the highly perforated micropores (Figures 2e and S10).[54] Response and recovery times were ∼80 ms at 10% strain, increasing to 500/465 and 664/626 ms at 20 and 30% strain, respectively (Figure S11). No evidence of skin irritation was observed during application to human skin (Figure S12), suggesting compatibility for wearable use.

Physiological Signal Analysis across Canine Breeds and Activities

To evaluate the performance of the smart garment, we monitored two canine breeds (a Labrador and a Boxer) during resting, walking, and running activities (Movie S1). Commercially available garments in various sizes and colors were adapted into smart garments to ensure proper fit and comfort across breeds. Figure 3a illustrates the experimental setup, where both animals wore the smart garments without notable discomfort, scratching, or avoidance behaviors (Figure 3b).

Figure 3c shows respiration trends across activities. In the Labrador, respiration at rest averaged 18 breaths per minute (bpm) with an amplitude of 12.6% ($\Delta R/R_0$), reflecting deep, slow breathing. Occasional pauses following deep breaths were observed (Figure S13). During walking, respiration increased to 58 bpm with an amplitude of 12.5%, while running elevated the rate to ∼160 bpm with a reduced amplitude of 9.2%, characteristic of panting for thermoregulation.[55,56] In contrast, the Boxer displayed a higher baseline respiration rate and lower amplitude even at rest, consistent with its breed-specific tendency toward rapid, shallow breathing. Transition to walking and running produced only modest changes in rate and amplitude compared to the Labrador. These differences emphasize the importance of breed-specific baselines when interpreting physiological data (Figure 3d).

An accelerometer and a temperature sensor were used to confirm that activity level and surface temperature were consistent across each activity condition (e.g., resting, walking, and running) and did not provide additional discriminative information for the

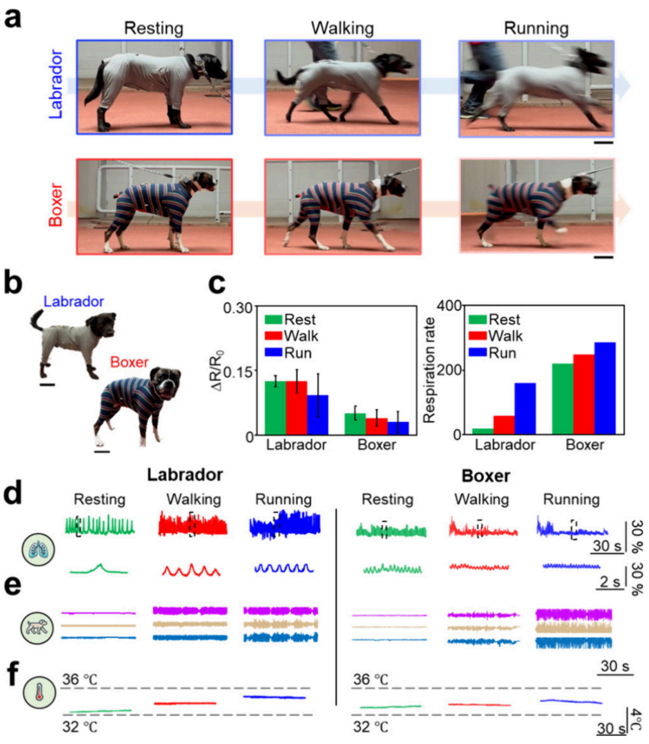

Figure 3. Physiological signal analysis of dogs under different activity states. (a) Sequential images of Labrador and Boxer with smart garment during resting, walking, and running. Scale bar, 20 cm. (b) Labrador and Boxer, wearing smart garment. Scale bar, 15 cm. (c) Bar graphs showing (left) the relative change in respiratory signal amplitude ($\Delta R/R_0$) and (right) respiration rate across activities for both breeds. (d) Time-domain respiration signals for Labrador and Boxer under each condition, with expanded views highlighting waveform features. (e) Accelerometer data confirming activity transitions. (f) Temperature readings during each activity state.

respiration measurements. Figure 3e highlights accelerometer data that captured activity-dependent motion, showing low signals at rest and progressively greater amplitudes during walking and running. The accelerometer was placed on the upper back to minimize motion artifacts for their use in coarse activity tagging (e.g., resting, walking, and running). Figure 3f shows surface body temperature trends, recording the skin-adjacent surface temperature at the body−garment interface, which gradually increases with activity and reflects physiological thermoregulation. Detailed datasets of key physiological parameters, including temperature and activity levels, showing no abrupt deviations across resting, walking, and running while wearing the smart garment, are provided in Figure S14. Collectively, these results demonstrate the system's capability to capture multimodal physiological signals—including respiration, motion, and temperature—under natural activity states. Such real-time monitoring may be particularly useful for elderly or recovering canines, supporting early detection of abnormalities and timely clinical intervention.

Respiration Classification Using ML/CNN Approaches

To support physiological pattern recognition and aid veterinary decision-making, we implemented AI-based analysis. Two canine breeds (Labrador and Boxer) were monitored under resting, walking, and running activities (Figure 4a), and representative signals are shown in Figure 4b. These data were compiled into a dataset for classification using ML/CNN models.

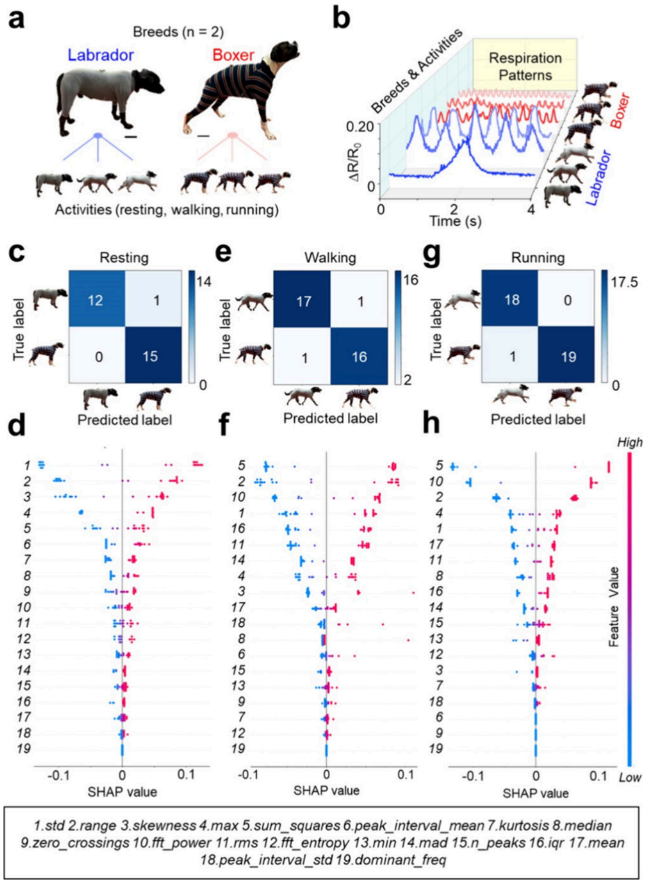

Figure 4. (a) Photographs of Labrador and Boxer with different activities (e.g., resting, walking, and running). Scale bar, 15 cm. (b) Respiratory signals of Labrador and Boxer during different activities (e.g., resting, walking, and running). Confusion matrices of Random Forest classifiers for Labrador and Boxer classification under (c) resting, (e) walking, and (g) running conditions. SHAP summary plots visualizing the impactful features for the corresponding activity states, including (d) resting, (f) walking, and (h) running.

For the resting condition, RF achieved the best performance with an accuracy of 96.4%, an AUC-ROC of 0.9795,[57] and an AP of 0.9815, outperforming DT (82.1% accuracy) and XGBoost (85.7%) (Table S3, Figure S15). Confusion matrices showed RF yielded only one false negative and no false positives for Boxer. The false negative rates (FNR) for Labrador misclassification were: RF, 7.7%; DT, 15.4%; XGBoost, 15.4% (Figures 4c and S16). SHAP analysis revealed that statistical features such as standard deviation, maximum, and range contributed most strongly to RF model predictions (Figures 4d, S17 and S18), highlighting subtle breed-specific differences in breathing variability during rest.

For the walking condition, XGBoost performed slightly better than RF, achieving the highest AUC-ROC (0.9526 [95.0% CI: 0.9030−0.9342]) and AP (0.9690), though RF matched its accuracy (94.3%) and exhibited nearly identical sensitivity/specificity (0.9412/0.9444) (Table S4, Figure S19). DT showed lower performance (91.4% accuracy, AUC-ROC 0.9134, AP 0.8843). Confusion matrices confirmed high true positive and true negative rates (~94%) for both RF and XGBoost, with identical Labrador misclassification rates (FNR = 5.6%) across classifiers (Figures 4e and S20). SHAP interpretation of RF indicated that energy- and frequency-domain features (sum of squares, Fast Fourier Transform (FFT)_power, range) were the dominant contributors during walking (Figures 4f, S21 and S22), reflecting increased signal complexity at moderate activity.

For the running condition, RF again outperformed the others with an accuracy of 97.4%, AUC-ROC of 0.9889 [95.0% CI: 0.9889−0.9910], and AP of 0.9917 (Table S5, Figure S23). DT matched RF in accuracy but showed lower AUC-ROC (0.9750) and AP (0.9763). XGBoost performance declined notably (92.1% accuracy, AUC-ROC 0.9000, AP 0.8476). Confusion matrices revealed that RF and DT each misclassified one Boxer sample (sensitivity = 95.0%), whereas XGBoost perfectly classified all Boxers but misclassified three Labrador samples (FNR = 16.7%) (Figures 4g and S24). SHAP analysis for RF again emphasized energy- and amplitude-based features (sum of squares, FFT_power, range) as the key discriminators (Figures 4h, S25 and S26).

In summary, while XGBoost showed marginally better performance during walking, RF consistently delivered the highest or comparable results across all conditions, demonstrating the most robust and reliable model for breed-specific respiratory classification.

CONCLUSIONS

In this study, we developed a smart garment for canine health monitoring, enabling non-invasive tracking of respiration, body temperature, and motion across different breeds and activity states. Validation with Labrador and Boxer dogs demonstrated the system's ability to detect physiological changes during resting, walking, and running. Distinct breed-specific differences were captured, particularly in respiration rate, amplitude, and variability, along with corresponding changes in motion and temperature. Furthermore, deep learning models classified respiratory patterns with accuracies exceeding 94.3%, highlighting the potential for diagnostic applications.

These findings underscore the value of smart garments in enabling breed- and activity-specific monitoring, laying the foundation for personalized and preventative veterinary care. Nonetheless, respiratory signals may be influenced by confounding factors such as temperature, humidity, stress, or motion artifacts caused by abrupt animal movements, which can mask subtle respiratory signals. Future studies will include larger and more diverse canine cohorts to improve statistical power and enable population-level generalization of physiological findings. Future work will evaluate the smart clothing's robustness under rainy conditions as well as other challenging outdoor scenarios, including high humidity, temperature extremes, prolonged wear, and environmental contaminants, to assess potential artifacts and ensure reliable performance in diverse real-world settings

Overall, this work establishes a practical approach to real-time veterinary health monitoring. By enabling early detection of abnormalities and reducing unnecessary clinical visits, smart garments hold promise to transform routine canine care. Importantly, the design concept is not limited to dogs but can be adapted to other companion animals such as cats or rabbits, extending its relevance to broader animal healthcare.

EXPERIMENTAL SECTION

Materials

The average diameter and length of the MWCNTs (Cheap Tubes, Inc.; purity >95 wt %) were measured as 10−20 nm and 10−30 μm, respectively. The MWCNTs were blended with isopropanol at a weight ratio of 0.5 wt % and sonicated for an hour to produce a uniform suspension through untangling. A commercial textile band, garment, and super fabric were purchased from Xpand, Amazon and lessemf.

Fabrication of the Spongy CNT Foam

The steam-etching system comprised a pressure cooker (Instant Pot Duo; Instant Brands, Inc.) partially filled with approximately 500 g of water and equipped with an internal raised stage to hold the PDMS-coated substrate above the liquid surface (Figure S27). Glass substrates were cleaned sequentially with acetone, isopropyl alcohol, and deionized water, followed by drying. A PDMS prepolymer prepared by mixing the base and curing agent at a 10:1 weight ratio was spin-coated onto the cleaned glass. The coated substrates were positioned on the elevated stage at the center of the chamber. Steam etching process was conducted at 120 °C under a pressure of 15 psi for 15−30 min, inducing the formation of micropores with diameters in the range of ~5−50 μm over a total processing area of approximately 4 × 3 in.^{2}. It was then subjected to oxygen plasma for 10 min to create a hydrophilic surface and immersed in a solution of CNTs. This facilitated the absorption and deposition of the CNTs throughout the perforated micropores. The resulting spongy CNT foam was cut to the desired size for use.

Finite Element Analysis (FEA)

A commercially available standard software, the ABAQUS package, was used for FEA. The serpentine structures were modeled with a linear elastic model with modulus of 5 GPa and Poisson's ratio of 0.3. Strain values exceeding the maximum strain contours of 40% were colored red to aid in visual analysis.

Fabrication of Devices

Schematic diagrams and PCB layouts were created using commercial software (Autodesk Eagle, Version 9.6.2). The smart textile band incorporates a three-layer stacked, three-island fPCB design, integrating commercially available electronic components. The first island includes a three-axis digital accelerometer and a thermometer. The second island contains the battery charging circuit and voltage regulators, while the third island houses the BLE SoC and indicator LEDs. Customized firmware was programmed into the BLE SoC. Surface-mount components were assembled onto the fPCB using solder paste (SMDLTLFP10T5, Chip Quik), a heat gun (Int866, Aqyue), and a hot plate (MHP30, Miniware). A commercial textile band (Magnetic Urban Elastic Belt, Xpand) was integrated between the first and second fPCB layers. The complete assembly was encapsulated in a soft, waterproof elastomer (Ecoflex 00-35, Smooth-On) to ensure environmental protection, mechanical durability, and flexibility.

Encapsulation Process

A mold was designed using commercial 3D CAD software (Autodesk Fusion 360, Version 2.0) and fabricated with a stereolithography 3D printer (Form3, Formlabs). Prior to encapsulation, a silicone release agent (Ease Release 200, Mann Release Technologies) was applied to the mold surfaces. The encapsulation process was performed with the fully assembled sensor module and textile neckband placed inside the mold. A soft elastomer (Ecoflex 00-35, Smooth-On) was used as the encapsulation material to provide mechanical protection and flexibility.

Mechanical and Electrical Characterizations

The spongy CNT foam was cut to a size of 2 cm × 7.5 cm for mechanical testing using a mechanical testing system (Mark-10) to obtain its stress-strain curve. The resistance of the spongy CNT foam was measured using a source meter (Keithley 2400; Tektronix, Inc.) for electrical testing. The structural details of the spongy CNT foam were analyzed using a high-resolution SEM (S-4800; Hitachi, Inc.).

Gauge factor (*GF*): Gauge factor is defined by the following eq 1:

$$\mathrm{GF} = \left(\Delta R/R_0\right)/\varepsilon \tag{1}$$

where R_0, ΔR, and ε are the initial resistance before stretching, difference of resistance under stretching, and applied strain, respectively. The GF of the spongy CNT foam was obtained from a linear fitting divided by each strain of 10%.

Mechanical and Electrical Hysteresis

The mechanical and electrical hysteresis of the spongy CNT foam was evaluated by plotting the $\Delta R/R_0$ versus strain curves, with the resistance of each cycle set as the initial value. The extent of hysteresis was determined from the width of the hysteresis loop. The areal variation between the loading and unloading states of relative electrical signal change versus strain was quantitatively defined as electrical hysteresis and by the following eq 2:

$$H_{\mathrm{E}} = \frac{|A_{\mathrm{L}} - A_{\mathrm{U}}|}{A_{\mathrm{U}}} \times 100\,\% \tag{2}$$

where A_{L} and A_{U} are the areas of relative electrical signal change versus strain in the loading and unloading states, respectively. Mechanical hysteresis (H_{M}) was defined as the areal difference under stress-strain curves during loading-unloading cycles and computed by the following eq 3:

$$H_{\mathrm{M}} = \frac{|A_{\mathrm{L}} - A_{\mathrm{U}}|}{A_{\mathrm{U}}} \times 100\,\% \tag{3}$$

where A_{L} and A_{U} are the area under the stress-strain graph in loading and unloading states, respectively. All the animal studies were conducted in compliance with the university regulations and approved by the Institutional Review Board (IRB protocol #: 202212-009).

Skin Irritation Testing

Inflammation accompanied by erythema, which changes the concentrations of hemoglobin, is a common response after irritation of the human skin. Line-scan hyperspectral images (hypercube) of the human skin were obtained using a monochrome camera (GS3-U3-120S6M-C; FLIR), with a slit width of 23 μm and groove density of 150 mm^{-1}. An LED light source with a color temperature of 6500 K (D65) was used as the illumination source. Spectral calibration of the spectrograph was performed using a xenon calibration light source that emitted multiple narrow peaks at specific wavelengths. A fixed focal length lens (MVL25M1; Navitar) was mainly used to image the skin, with a field of view as small as 10 mm × 10 mm. The same area was imaged with a smartphone camera (iPhone 11 Pro; Apple) to capture RGB images. The spongy CNT foam was applied onto the medial antebrachial cutaneous of the forearm for around 10 min. As a positive control, a 3 M tape was attached to the same area for 10 min. Images were acquired before and after the experiment for hemoglobin content comparison. A mechanical linear scan step was performed at 0.25 mm. The data was acquired using a custom MATLAB interface. A tissue reflectance spectral model was used to extract key hemodynamic parameters from the ground-truth hyperspectral image. The theory of radiative transport and robust approximations (e.g., diffusion, Born, and empirical modeling) was used to model light propagation in tissue. The intensity reflected from a biological sample can be expressed as a function of λ in the visible range:

$$I_{\mathrm{R}}(\lambda) = \left[b_1\left(\frac{\lambda}{\lambda_0}\right)^{b_2} + b_3\left(\frac{\lambda}{\lambda_0}\right)^{-4}\right]\exp[-b_4 \times \{b_5 \times \varepsilon_{\mathrm{HbO_2}}(\lambda) + (1-b_5) \times \varepsilon_{\mathrm{Hb}}(\lambda)\}] \tag{4}$$

where b_1, b_2, and b_3 are associated with the scattering (Mie or Rayleigh) contributions at $\lambda_0 = 800$ nm, $\varepsilon_{\mathrm{HbO2}}$ (λ) denotes the absorption coefficient of oxygenated hemoglobin ($\mathrm{HbO_2}$), $\varepsilon_{\mathrm{Hb}}$ (λ) denotes the absorption coefficient of deoxygenated hemoglobin (H_{b}), b_4 is the hemoglobin concentration multiplied by the optical pathlength, and b_5 is the blood oxygen saturation ($\mathrm{sPO_2}$). In the study, the hemoglobin contents multiplied by the optical pathlength (b_4) was used to indicate the level of skin irritation by eq 4. All fitting parameters were computed using the simplex search (Nelder-Mead) algorithm.

Development of ML/CNN Algorithms

Respiration data were collected as a dataset and used as input for ML/CNN models trained to classify distinct activity classes (Figure S28a). Three binary classification tasks were designed to evaluate whether respiration-derived features from smart garment can distinguish between breeds during identical physical activities. Each task focused on classifying between Labrador and Boxer under one of three activity conditions (e.g., resting, walking, and running). Breathing signals were acquired using the smart garment, which captured resistance changes ($\Delta R/R_0$) associated with thoracic expansion and contraction. Raw time-series signals were manually annotated using activity logs and segmented into labeled intervals, which were then divided into non-overlapping 6-s windows to standardize input lengths and increase data volume for training. Two complementary feature extraction strategies were employed to characterize breathing signals: a ML-based statistical approach and a deep learning-based CNN approach. In the ML-based statistical pipeline, each 6-s breathing segment was transformed into a structured feature vector based on four main categories: (1) Peak and Temporal Features: peak-to-peak amplitude, signal slope (first derivative), number of peaks, inter-peak intervals, signal range, and zero crossings, (2) Energy-Related Features: root mean square (RMS), sum of squares, and total FFT power, (3) Statistical Features: mean, median, standard deviation, interquartile range (IQR), median absolute deviation (MAD), minimum, maximum, skewness, and kurtosis, and (4) Frequency Domain Features: dominant frequency and spectral entropy derived from FFT analysis. In the CNN-based pipeline, each raw 6-s window of 1D respiration signal was fed into a custom-designed convolutional neural network. The architecture consisted of stacked 1D convolutional layers with Rectified Linear Unit (ReLU) activation and batch normalization, followed by global average pooling to generate fixed-length latent embeddings, a design commonly adopted in signal and imaging applications for its efficiency and robustness.[58] These learned representations captured temporal dynamics in the breathing signal without relying on handcrafted features.[59] To ensure fair and leakage-free evaluation, the full dataset was initially split into 80% training and 20% hold-out test sets. Both CNN-derived embeddings and handcrafted statistical features were extracted exclusively from the training set and used as inputs to the classifiers. Handcrafted features included peak-related, energy-based, statistical, and frequency-domain metrics. The resulting feature vectors from both pipelines were then used as inputs to three supervised classifiers (e.g., XGBoost, RF, and DT), which were chosen for their complementary strengths in handling non-linear relationships, feature interactions, and interpretability, thereby enabling a direct comparison between handcrafted and learned representations (Figure S28b).[60−62]

Machine Learning

All features were normalized to the [0, 1] range using min-max scaling, followed by the model training. While tree-based models are generally robust to unscaled inputs, normalization was applied for consistency and to support potential future use with other algorithms. For each classifier, 10-fold stratified cross-validation was conducted within the 80% training set to assess performance and identify optimal feature-classifier combinations. Final model performance was assessed using the independent 20% test set, based on standard classification metrics: accuracy, sensitivity (recall), specificity, positive predictive value (PPV), negative predictive value (NPV), and AUC-ROC.[63]

Additionally, confusion matrices and precision−recall (PR) curves were generated to provide class-wise performance insights. To interpret model behavior and identify key contributors, SHAP values were computed for tree-based classifiers, enabling transparent visualization of each feature's contribution to predictions.[64] All preprocessing, feature extraction, and classification steps were implemented in Python using NumPy, SciPy, and Scikit-learn.[65,66]

■ ASSOCIATED CONTENT

Supporting Information

The Supporting Information is available free of charge at https://pubs.acs.org/doi/10.1021/acssensors.5c03783.

> Figure S1: Fabrication process of smart garment; Figure S2: FEA result of serpentine interconnectors, images of steam-etching setup, spongy PDMS and pore distributions, scale bars: 4 and 1 cm; Figure S3: layout of the flexible printed circuit board (fPCB) and block diagram; Figure S4: SEM images of the spongy-like strain sensor, with different infiltration cycles, scale bar: 5 μm, stress−strain curve of the spongy-like strain sensor with different infiltration cycles, resistance and $\Delta R/R_0$ of the spongy-like strain sensor with different infiltration cycles, gauge factor with the strain of the spongy-like strain sensor, $\Delta R/R_0$ of the spongy-like strain sensor as a function of different infiltration cycles; Figure S5: comparison of GF and maximum working strain range among various stretchable strain sensors; Figure S6: strain sensing range and $\Delta R/R_0$ of the spongy-like strain sensor with the different sample size; Figure S7: $\Delta R/R_0$ of the spongy-like strain sensor during 2000 stretching-releasing cycles at 90% strain; Figure S8: photographs and SEM images of the spongy CNT foam under stretching, scale bars, 5 mm, 150 μm, 5 μm; Figure S9: $\Delta R/R_0$ observed in the spongy-like strain sensor during pressing; Figure S10: H_M and H_E of the spongy CNT foam; Figure S11: response/recovery time of the spongy-like strain sensor; Figure S12: RGB images of skin before experiments (control), after applying spongy-like strain sensor and 3M tape (left column), hemoglobin map measured with hyperspectral line-scanning system (right column), scale bar: 3 mm, average hemoglobin contents of a sampled area *a*) shown in bar graph; Figure S13: real-time monitoring of respiration, scale bar: 1 cm; Figure S14: time series data from temperature and three-axis acceleration, capturing activities such as resting, walking and running; Figure S15: ROC and precision−recall curves of Random Forest, Decision Tree, and XGBoost classifiers under resting condition; Figure S16: confusion matrices of Decision Tree and XGBoost classifiers for resting-state classification; Figure S17: top 10 most important features identified by Random Forest, Decision Tree, and XGBoost classifiers under resting condition; Figure S18: SHAP summary plots for Decision Tree and XGBoost models under resting condition; Figure S19: ROC and precision−recall curves of Random Forest, Decision Tree, and XGBoost classifiers under walking condition; Figure S20: confusion matrices of Decision Tree and XGBoost classifiers for walking-state classification; Figure S21: top 10 most important features identified by Random Forest, Decision Tree, and XGBoost classifiers under walking condition; Figure S22: SHAP summary plots for Decision Tree and XGBoost models under walking condition; Figure S23: ROC and precision−recall curves of Random Forest, Decision Tree, and XGBoost classifiers under running condition; Figure S24: confusion matrices of Decision Tree and XGBoost classifiers for running-state classification; Figure S25: Top 10 most important features identified by Random Forest, Decision Tree, and XGBoost classifiers under running condition; Figure S26: SHAP summary plots for Decision Tree and XGBoost models under running condition; Figure S27: schematic illustration and photograph of the fabrication setup; Figure S28: end-to end pipeline for respiration-based breed classification using CNN-/ML-assisted feature extraction and ML classifiers, raw respiration signals acquired from smart clothing sensors are segmented into 6-s multivariate time windows, which are then processed through two feature extraction pipelines: (i) handcrafted statistical, temporal, energy, and frequency-domain features and (ii) learned embeddings from a 1D convolutional neural network (CNN), these features vectors are input into supervised ML classifiers to perform binary classification of dog breed (Labrador vs Boxer) under each activity stage (resting, walking, running), comparison of classifier structures used in this study, XGBoost performs residual-based boosting across weak learners, Random Forest aggregates predictions from independently trained decision tress; and the baseline Decision Tree provides a single hierarchical split-based prediction; Table S1: overview of veterinary wearable systems used for canine respiration monitoring; Table S2: comparison of fabrication methods for porous structures; Table S3: performance metrics for Labrador vs Boxer classification under the resting condition; Table S4: performance metrics for Labrador vs Boxer classification under the walking condition; and Table S5: performance metrics for Labrador vs Boxer classification under the running condition (DOCX)
>
> Movie S1: Real-time monitoring of activities (e.g., resting, walking, and running) of dogs (MP4)

■ AUTHOR INFORMATION

Corresponding Authors

Rachel K. Surowiec − *Weldon School of Biomedical Engineering, Purdue University, West Lafayette, Indiana 47907, United States;* Email: rsurowie@purdue.edu

Luis Dos Santos − *Department of Veterinary Clinical Sciences, Purdue University, West Lafayette, Indiana 47907, United States;* Email: dossantos@purdue.edu

Chi Hwan Lee − *Weldon School of Biomedical Engineering, Purdue University, West Lafayette, Indiana 47907, United States; Center for Implantable Devices, Purdue University , West Lafayette, Indiana 47907, United States; Birck Nanotechnology Center, Purdue University, West Lafayette, Indiana 47907, United States; School of Mechanical Engineering, Purdue University, West Lafayette, Indiana 47907, United States; School of Materials Engineering, Purdue University , West Lafayette, Indiana 47907, United States; Elmore Family School of Electrical and Computer Engineering, Purdue University, West Lafayette, Indiana 47907, United States;* orcid.org/0000-0002-4868-7054; Email: lee2270@purdue.edu

Authors

Seokkyoon Hong – *Weldon School of Biomedical Engineering, Purdue University, West Lafayette, Indiana 47907, United States;* orcid.org/0009-0007-6540-0389

Taewoong Park – *Weldon School of Biomedical Engineering, Purdue University, West Lafayette, Indiana 47907, United States*

Youngjun Lee – *Weldon School of Biomedical Engineering, Purdue University, West Lafayette, Indiana 47907, United States*

Juan C. Mesa – *Weldon School of Biomedical Engineering, Purdue University, West Lafayette, Indiana 47907, United States; Center for Implantable Devices, Purdue University , West Lafayette, Indiana 47907, United States; Birck Nanotechnology Center, Purdue University, West Lafayette, Indiana 47907, United States*

Tianhao Yu – *School of Mechanical Engineering, Purdue University, West Lafayette, Indiana 47907, United States;* orcid.org/0000-0001-9637-352X

Yuhyun Ji – *Weldon School of Biomedical Engineering, Purdue University, West Lafayette, Indiana 47907, United States*

Junsang Lee – *Weldon School of Biomedical Engineering, Purdue University, West Lafayette, Indiana 47907, United States*

Jinheon Jeong – *Weldon School of Biomedical Engineering, Purdue University, West Lafayette, Indiana 47907, United States*

Seok-Won Kang – *Department of Automotive Engineering, Yeungnam University, Gyeongbuk 38541, Republic of Korea;* orcid.org/0000-0003-2062-5297

Dong Rip Kim – *School of Mechanical Engineering, Hanyang University , Seoul 04763, Republic of Korea;* orcid.org/0000-0001-6398-9483

Young L. Kim – *Weldon School of Biomedical Engineering, Purdue University, West Lafayette, Indiana 47907, United States;* orcid.org/0000-0003-3796-9643

Hyowon Lee – *Weldon School of Biomedical Engineering, Purdue University, West Lafayette, Indiana 47907, United States; Center for Implantable Devices, Purdue University , West Lafayette, Indiana 47907, United States; Birck Nanotechnology Center, Purdue University, West Lafayette, Indiana 47907, United States;* orcid.org/0000-0001-7628-1441

Complete contact information is available at: https://pubs.acs.org/doi/10.1021/acssensors.5c03783

Author Contributions

‖S.H., T.P., and Y.L. contributed equally to this work.

Notes

The authors declare no competing financial interest.

ACKNOWLEDGMENTS

The research reported in this publication was supported in part by the National Institute of Biomedical Imaging and Bioengineering of the National Institutes of Health under Award Number R21EB034879, which contributed to the fabrication aspects of this work. C.H.L. acknowledges support from the Leslie A. Geddes and University Faculty Scholar endowment.

REFERENCES

(1) Creevy, K. E.; Akey, J. M.; Kaeberlein, M.; Promislow, D. E. L.; Barnett, B. G.; Benton, B.; Borenstein, E.; Castelhano, M. G.; Chou, L.; Collins, D.; Coleman, A. E.; Crowder, K.; Dunbar, M. D.; Evans, J.; Fajt, V. R.; Fitzpatrick, A. L.; Jeffery, U.; Jonlin, E. C.; Karlsson, E. K.; Kerr, K. F.; Lee, H.; Levine, J. M.; Ma, J.; McClelland, R. L.; McNulty, K. E.; Morrill, K.; Nam, Y.; Ruple, A.; Schwartz, S. M.; Shrager, S.; Snyder-Mackler, N.; Thistlethwaite, W.; Tinkle, A. K.; Tolbert, M. K.; Urfer, S. R.; Wilfond, B. S. An open science study of ageing in companion dogs. *Nature* **2022**, *602*, 51–57.

(2) Irvine, L.; Cilia, L. More-than-human families: Pets, people, and practices in multispecies households. *Sociol. Compass* **2017**, *11* (2), No. e12455.

(3) Ahmad, R. u. S.; Khan, M. S.; Hilal, M. E.; Khan, B.; Zhang, Y.; Khoo, B. L. Advancements in wearable heart sounds devices for the monitoring of cardiovascular diseases. *SmartMat* **2025**, *6*, No. e1311.

(4) Mahato, K.; Saha, T.; Ding, S.; Sandhu, S. S.; Chang, A. Y.; Wang, J. Hybrid multimodal wearable sensors for comprehensive health monitoring. *Nat. Electron.* **2024**, *7*, 735–750.

(5) Li, H.; Gong, H.; Wong, T. H.; Zhou, J.; Wang, Y.; Lin, L.; Dou, Y.; Jia, H.; Huang, X.; Gao, Z.; Shi, R.; Huang, Y.; Chen, Z.; PARK, W.; Li, J. Y.; Chu, H.; Jia, S.; Wu, H.; Wu, M.; Liu, Y.; Li, D.; Li, J.; Xu, G.; Chang, T.; Zhang, B.; Gao, Y.; Su, J.; Bai, H.; Hu, J.; Yiu, C. K.; Xu, C.; Hu, W.; Huang, J.; Chang, L.; Yu, X. Wireless, battery-free, multifunctional integrated bioelectronics for respiratory pathogens monitoring and severity evaluation. *Nat. Commun.* **2023**, *14*, 7539.

(6) Smith, K. F.; Quinn, R. L.; Rahilly, L. J. Biomarkers for differentiation of causes of respiratory distress in dogs and cats: part 1–cardiac diseases and pulmonary hypertension. *J. Vet. Emerg. Crit. Care* **2015**, *25*, 311–329.

(7) Schmid, C.; Steiner, A. R.; Spielhofer, L.; Galfetti, M.; Rentsch, N.; Bogdanov, N.; Vogel, J.; Hofmann-Lehmann, R.; Hartnack, S.; Astakhov, G.; Furrer, R.; Bogdanova, A.; Reichler, I. M. Anatomical, functional, and blood-born predictors of severity of brachycephalic obstructive airway syndrome severity in French Bulldogs. *Front. Vet. Sci.* **2025**, *11*, No. 1486440.

(8) Fastrès, A.; Roels, E.; Vangrinsven, E.; Taminiau, B.; Jabri, H.; Bolen, G.; Merveille, A. C.; Tutunaru, A. C.; Moyse, E.; Daube, G.; Clercx, C. Assessment of the lung microbiota in dogs: influence of the type of breed, living conditions and canine idiopathic pulmonary fibrosis. *BMC Microbiol.* **2020**, *20*, 84.

(9) Protopopova, A.; Hall, N. J.; Brown, K. M.; Andrukonis, A. S.; Hekman, J. P.; Olsson, I. A. S. Behavioral predictors of subsequent respiratory illness signs in dogs admitted to an animal shelter. *PLoS One* **2019**, *14*, No. e0224252.

(10) Fischer-Tenhagen, C.; Meier, J.; Pohl, A. "Do not look at me like that": Is the facial expression score reliable and accurate to evaluate pain in large domestic animals? A systematic review. *Front. Vet. Sci.* **2022**, *9*, No. 1002681.

(11) Dev, S. P.; Hillmer, M. D.; Ferri, M. Arterial puncture for blood gas analysis. *N. Engl. J. Med.* **2011**, *364*, No. e7.

(12) Gray, S.; Burkitt Creedon, J. M.; Davis, H. Blood gas analysis. *Advanced monitoring and procedures for small animal emergency and critical care*; John Wiley & Sons, Inc., 2023; 339−346.

(13) Marshall, M. Capnography in dogs. *Compend. Contin. Educ. Pract. Vet.* **2004**, *26*, 761–778.

(14) Wilson, D. V.; Shih, A. C. Anesthetic emergencies and resuscitation. *Veterinary Anesthesia and Analgesia*: *The Fifth Edition of Lumb and Jones*; John Wiley & Sons, Inc., 2015, 114−129.

(15) Hafke-Dys, H.; Bręborowicz, A.; Kleka, P.; Kociński, J.; Biniakowski, A.; Wu, A. G. The accuracy of lung auscultation in the practice of physicians and medical students. *PLoS One* **2019**, *14*, No. e0220606.

(16) Lin, C. H.; Johnson, L. R.; Chang, W. T.; Lo, P. Y.; Chen, H. W.; Wu, H. D. Quantifiable features of a tidal breathing phenotype in dogs with severe bronchomalacia diagnosed by bronchoscopy. *Vet. Q.* **2023**, *43*, 1–10.

(17) Kisielinski, K.; Giboni, P.; Prescher, A.; Klosterhalfen, B.; Graessel, D.; Funken, S.; Kempski, O.; Hirsch, O. Is a mask that covers the mouth and nose free from undesirable side effects in everyday use and free of potential hazards? *Int. J. Environ. Res. Public Health* **2021**, *18*, 4344.

(18) Nomoto, K.; Hashimoto, T.; Nagasawa, M.; Kikusui, T. Dog's breath rhythm was drawn into owner's breath rhythm. *Adv. Robot.* **2024**, *38*, 926–933.

(19) Rozanski, E. A.; Hoffman, A. M. Lung mechanics using plethysmography and spirometry. *Textbook of respiratory disease in dogs and cats*; Saunders: St Louis, 2004, 175−180.

(20) Elisheva, R. Adverse effects of prolonged mask use among healthcare professionals during COVID-19. *J. Infect. Dis. Epidemiol.* **2020**, *6*, 130.

(21) Neal, S. M.; Greenberg, M. J. Putting access to veterinary care on the map: a veterinary care accessibility index. *Front. Vet. Sci.* **2022**, *9*, No. 857644.

(22) Niemiec, R.; Champine, V.; Frey, D.; Lobdell, A.; Steele, A.; Vaiden, C.; Kogan, L.; Mertens, A. Veterinary and pet owner perspectives on addressing access to veterinary care and workforce challenges. *Front. Vet. Sci.* **2024**, *11*, No. 1419295.

(23) Luo, Y.; Abidian, M. R.; Ahn, J. H.; Akinwande, D.; Andrews, A. M.; Antonietti, M.; Bao, Z.; Berggren, M.; Berkey, C. A.; Bettinger, C. J.; Chen, J.; Chen, P.; Cheng, W.; Cheng, X.; Choi, S. J.; Chortos, A.; Dagdeviren, C.; Dauskardt, R. H.; Di, C. A.; Dickey, M. D.; Duan, X.; Facchetti, A.; Fan, Z.; Fang, Y.; Feng, J.; Feng, X.; Gao, H.; Gao, W.; Gong, X.; Guo, C. F.; Guo, X.; Hartel, M. C.; He, Z.; Ho, J. S.; Hu, Y.; Huang, Q.; Huang, Y.; Huo, F.; Hussain, M. M.; Javey, A.; Jeong, U.; Jiang, C.; Jiang, X.; Kang, J.; Karnaushenko, D.; Khademhosseini, A.; Kim, D. H.; Kim, I. D.; Kireev, D.; Kong, L.; Lee, C.; Lee, N. E.; Lee, P. S.; Lee, T. W.; Li, F.; Li, J.; Liang, C.; Lim, C. T.; Lin, Y.; Lipomi, D. J.; Liu, J.; Liu, K.; Liu, N.; Liu, R.; Liu, Y.; Liu, Y.; Liu, Z.; Liu, Z.; Loh, X. J.; Lu, N.; Lv, Z.; Magdassi, S.; Malliaras, G. G.; Matsuhisa, N.; Nathan, A.; Niu, S.; Pan, J.; Pang, C.; Pei, Q.; Peng, H.; Qi, D.; Ren, H.; Rogers, J. A.; Rowe, A.; Schmidt, O. G.; Sekitani, T.; Seo, D. G.; Shen, G.; Sheng, X.; Shi, Q.; Someya, T.; Song, Y.; Stavrinidou, E.; Su, M.; Sun, X.; Takei, K.; Tao, X. M.; Tee, B. C. K.; Thean, A. V. Y.; Trung, T. Q.; Wan, C.; Wang, H.; Wang, J.; Wang, M.; Wang, S.; Wang, T.; Wang, Z. L.; Weiss, P. S.; Wen, H.; Xu, S.; Xu, T.; Yan, H.; Yan, X.; Yang, H.; Yang, L.; Yang, S.; Yin, L.; Yu, C.; Yu, G.; Yu, J.; Yu, S. H.; Yu, X.; Zamburg, E.; Zhang, H.; Zhang, X.; Zhang, X.; Zhang, X.; Zhang, Y.; Zhang, Y.; Zhao, S.; Zhao, X.; Zheng, Y.; Zheng, Y. Q.; Zheng, Z.; Zhou, T.; Zhu, B.; Zhu, M.; Zhu, R.; Zhu, Y.; Zhu, Y.; Zou, G.; Chen, X. Technology roadmap for flexible sensors. *ACS Nano* **2023**, *17*, 5211–5295.

(24) Yang, J. C.; Mun, J.; Kwon, S. Y.; Park, S.; Bao, Z.; Park, S. Electronic skin: recent progress and future prospects for skin-attachable devices for health monitoring, robotics, and prosthetics. *Adv. Mater.* **2019**, *31*, No. 1904765.

(25) Liu, Y.; Putcha, A.; Lyda, G.; Peng, N.; Pai, S.; Nguyen, T.; Xing, S.; Peng, S.; Fan, Y.; Wu, Y.; Xie, W.; Bai, W. AI-boosted and motion-corrected, wireless near-infrared sensing system for continuously monitoring laryngeal muscles. *Proc. Natl. Acad. Sci. U. S. A.* **2024**, *121*, No. e2410750121.

(26) Zhang, Y.; Chen, H.; Song, Y. Wearable healthcare monitoring and therapeutic bioelectronics. *Wearable Electron.* **2025**, *2*, 18–22.

(27) Sneeringer, S.; Clancy, M. Incentivizing new veterinary pharmaceutical products to combat antibiotic resistance. *Appl. Econ. Perspect. Policy* **2020**, *42*, 653–673.

(28) Warhoe, J.; Simpson, S.; Goldblatt, B.; Zersen, K. Validation of Wireless Harness for Measuring Respiratory Rate, Heart Rate, and Body Temperature in Hospitalized Dogs. *Vet. Sci.* **2025**, *12*, 626.

(29) Rowlison de Ortiz, A.; Belda, B.; Hash, J.; Enomoto, M.; Robertson, J.; Lascelles, B. D. X. Initial exploration of the discriminatory ability of the PetPace collar to detect differences in activity and physiological variables between healthy and osteoarthritic dogs. *Front. Pain Res.* **2022**, *3*, No. 949877.

(30) Cotur, Y.; Kasimatis, M.; Kaisti, M.; Olenik, S.; Georgiou, C.; Güder, F. Stretchable composite acoustic transducer for wearable monitoring of vital signs. *Adv. Funct. Mater.* **2020**, *30*, No. 1910288.

(31) Cotur, Y.; Olenik, S.; Asfour, T.; Bruyns-Haylett, M.; Kasimatis, M.; Tanriverdi, U.; Gonzalez-Macia, L.; Lee, H. S.; Kozlov, A. S.; Güder, F. Bioinspired stretchable transducer for wearable continuous monitoring of respiratory patterns in humans and animals. *Adv. Mater.* **2022**, *34*, No. 2203310.

(32) Williams, E.; Hunton, V.; Boyd, J.; Carter, A. Effect of harness design on the biomechanics of domestic dogs (Canis lupus familiaris). *J. Appl. Anim. Welf. Sci.* **2025**, *28*, 301–317.

(33) Chao, F. L.; Feng, W. Z.; Shi, K. Smart Collar and Chest Strap Design for Rescue Dog through Multidisciplinary Approach. *Adv. Sci. Technol. Eng. Syst. J.* **2021**, *6*, 386–392.

(34) Carter, A.; McNally, D.; Roshier, A. Canine collars: an investigation of collar type and the forces applied to a simulated neck model. *Vet. Rec.* **2020**, *187*, No. e52.

(35) Cavalli, C.; Protopopova, A. Review of Collars, Harnesses, and Head Collars for Walking Dogs. *Animals* **2025**, *15*, No. 2162.

(36) Pauli, A. M.; Bentley, E.; Diehl, K. A.; Miller, P. E. Effects of the application of neck pressure by a collar or harness on intraocular pressure in dogs. *J. Am. Anim. Hosp. Assoc.* **2006**, *42*, 207–211.

(37) Martin, K. W.; Olsen, A. M.; Duncan, C. G.; Duerr, F. M. The method of attachment influences accelerometer-based activity data in dogs. *BMC Vet. Res.* **2016**, *13*, 48.

(38) Williamson, J. R.; Hess, A. R.; Smalt, C. J.; Sherrill, D. M.; Quatieri, T. F.; O'Brien, C. In Using collar-worn sensors to forecast thermal strain in military working dogs, *2016 IEEE 13th International Conference on Wearable and Implantable Body Sensor Networks (BSN)*; IEEE: San Francisco, CA, USA, 2016; 281−286.

(39) Belda, B.; Enomoto, M.; Case, B. C.; Lascelles, B. D. X. Initial evaluation of PetPace activity monitor. *Vet. J.* **2018**, *237*, 63–68.

(40) Nayebi, A.; Tipirneni, S.; Reddy, C. K.; Foreman, B.; Subbian, V. WindowSHAP: An efficient framework for explaining time-series classifiers based on Shapley values. *J. Biomed. Inform.* **2023**, *144*, No. 104438.

(41) Cai, Z.; Li, Z.; Ravaine, S.; He, M.; Song, Y.; Yin, Y.; Zheng, H.; Teng, J.; Zhang, A. From colloidal particles to photonic crystals: advances in self-assembly and their emerging applications. *Chem. Soc. Rev.* **2021**, *50*, 5898–5951.

(42) Hong, S.; Park, J.; Jeon, S. G.; Kim, K.; Park, S. H.; Shin, H. S.; Kim, B.; Jeon, S.; Song, J. Y. Monolithic Bi 1.5 Sb 0.5 Te 3 ternary alloys with a periodic 3D nanostructure for enhancing thermoelectric performance. *J. Mater. Chem. C* **2017**, *5*, 8974–8980.

(43) Kim, K.; Park, J.; Hong, S.; Park, S. H.; Jeon, S. G.; Ahn, C.; Song, J. Y.; Jeon, S. Anomalous thermoelectricity of pure ZnO from 3D continuous ultrathin nanoshell structures. *Nanoscale* **2018**, *10*, 3046–3052.

(44) Hong, S.; Zhang, H.; Lee, J.; Yu, T.; Cho, S.; Park, T.; Walsh, J.; Ji, Y.; Kim, J. J.; Lee, H.; Kim, D. R.; Xu, B.; Lee, C. H. Spongy Ag foam for soft and stretchable strain gauges. *ACS Appl. Mater. Interfaces* **2024**, *16*, 26613–26623.

(45) Yamada, T.; Hayamizu, Y.; Yamamoto, Y.; Yomogida, Y.; Izadi-Najafabadi, A.; Futaba, D. N.; Hata, K. A stretchable carbon nanotube strain sensor for human-motion detection. *Nat. Nanotechnol.* **2011**, *6*, 296–301.

(46) Ahuja, P.; Akiyama, S.; Ujjain, S. K.; Kukobat, R.; Vallejos-Burgos, F.; Futamura, R.; Hayashi, T.; Kimura, M.; Tomanek, D.; Kaneko, K. A water-resilient carbon nanotube based strain sensor for monitoring structural integrity. *J. Mater. Chem. A* **2019**, *7*, 19996–20005.

(47) Wang, X.; Li, J.; Song, H.; Huang, H.; Gou, J. Highly stretchable and wearable strain sensor based on printable carbon nanotube layers/polydimethylsiloxane composites with adjustable sensitivity. *ACS Appl. Mater. Interfaces* **2018**, *10*, 7371–7380.

(48) Hong, S.; Lee, J.; Park, T.; Jeong, J.; Lee, J.; Joo, H.; Mesa, J. C.; Alston, C. B.; Ji, Y.; Vega, S. R.; Barinaga, C.; Yi, J.; Lee, Y.; Kim, J.; Won, K. J.; Solorio, L.; Kim, Y. L.; Lee, H.; Kim, D. R.; Lee, C. H.

Spider Silk-Inspired Conductive Hydrogels for Enhanced Toughness and Environmental Resilience via Dense Hierarchical Structuring. *Adv. Sci.* **2025**, *12*, No. 2500397.

(49) Chang, T.; Akin, S.; Cho, S.; Lee, J.; Lee, S. A.; Park, T.; Hong, S.; Yu, T.; Ji, Y.; Yi, J. In situ spray polymerization of conductive polymers for personalized E-textiles. *ACS Nano* **2023**, *17*, 22733–22743.

(50) Hong, S.; Park, T.; Lee, J.; Ji, Y.; Dai, Y.; Yi, J.; Kim, J. J.; Kim, D. R.; Lee, C. H. Tough conductive organohydrogel for wearable sensing in extreme environmental conditions. *Adv. Mater. Technol.* **2024**, *9*, No. 2301398.

(51) Dahiya, A. S.; Gil, T.; Thireau, J.; Azemard, N.; Lacampagne, A.; Charlot, B.; Todri-Sanial, A. 1D nanomaterial-based highly stretchable strain sensors for human movement monitoring and human–robotic interactive systems. *Adv. Electron. Mater.* **2020**, *6*, No. 2000547.

(52) Hong, S.; Park, T.; Lee, J.; Ji, Y.; Walsh, J.; Yu, T.; Park, J. Y.; Lim, J.; Benito Alston, C.; Solorio, L.; Lee, H.; Kim, Y. L.; Kim, D. R.; Lee, C. H. Rapid self-healing hydrogel with ultralow electrical hysteresis for wearable sensing. *ACS Sens.* **2024**, *9*, 662–673.

(53) Hong, S.; Yu, T.; Wang, Z.; Lee, C. H. Biomaterials for reliable wearable health monitoring: Applications in skin and eye integration. *Biomaterials* **2025**, *314*, No. 122862.

(54) Kwon, D.; Lee, T. I.; Shim, J.; Ryu, S.; Kim, M. S.; Kim, S.; Kim, T. S.; Park, I. Highly sensitive, flexible, and wearable pressure sensor based on a giant piezocapacitive effect of three-dimensional microporous elastomeric dielectric layer. *ACS Appl. Mater. Interfaces* **2016**, *8*, 16922–16931.

(55) Johnson, S. I.; McMichael, M.; White, G. Heatstroke in small animal medicine: a clinical practice review. *J. Vet. Emerg. Crit. Care* **2006**, *16*, 112–119.

(56) Robertshaw, D. Mechanisms for the control of respiratory evaporative heat loss in panting animals. *J. Appl. Physiol.* **2006**, *101*, 664–668.

(57) Kang, Y. J.; Arafa, H. M.; Yoo, J.-Y.; Kantarcigil, C.; Kim, J.-T.; Jeong, H.; Yoo, S.; Oh, S.; Kim, J.; Wu, C. Soft skin-interfaced mechano-acoustic sensors for real-time monitoring and patient feedback on respiratory and swallowing biomechanics. *npj Digit. Med.* **2022**, *5*, 147.

(58) Kiranyaz, S.; Ince, T.; Gabbouj, M. Real-time patient-specific ECG classification by 1-D convolutional neural networks. *IEEE Trans. Biomed. Eng.* **2016**, *63*, 664–675.

(59) Ismail Fawaz, H.; Forestier, G.; Weber, J.; Idoumghar, L.; Muller, P. A. Deep learning for time series classification: a review. *Data Min. Knowl. Discov.* **2019**, *33*, 917–963.

(60) Chen, T.; He, T.; Benesty, M.; Khotilovich, V.; Tang, Y.; Cho, H.; Chen, K. ; Xgboost: extreme gradient boosting. *R package version 0.4-2*. 2015; *1*, 1−4.

(61) Priyam, A.; Abhijeeta, G. R.; Rathee, A.; Srivastava, S. Comparative analysis of decision tree classification algorithms. *Int. J. Curr. Eng. Technol.* **2013**, *3*, 334–337.

(62) Rigatti, S. J. Random forest. *J. Insur. Med.* **2017**, *47*, 31–39.

(63) De Hond, A. A.; Steyerberg, E. W.; Van Calster, B. Interpreting area under the receiver operating characteristic curve. *Lancet Digit. Health* **2022**, *4*, e853–e855.

(64) Nohara, Y.; Matsumoto, K.; Soejima, H.; Nakashima, N. Explanation of machine learning models using shapley additive explanation and application for real data in hospital. *Comput. Methods Programs Biomed.* **2022**, *214*, No. 106584.

(65) McKinney, W. pandas: a foundational Python library for data analysis and statistics. *Python for high performance and scientific computing*. 2011; *14*, 1−9.

(66) Pedregosa, F.; Varoquaux, G.; Gramfort, A.; Michel, V.; Thirion, B.; Grisel, O.; Blondel, M.; Prettenhofer, P.; Weiss, R.; Dubourg, V. Scikit-learn: Machine learning in Python. *J. Mach. Learn. Res.* **2011**, *12*, 2825–2830.

https://doi.org/10.1021/acssensors.5c03783
ACS Sens. XXXX, XXX, XXX−XXX